GJI Marine geosciences and applied geophysics

A statistical strategy for ambient seismic wavefield analysis: investigating correlations to a hydrocarbon reservoir

Nima Riahi,[1] Alexander Goertz,[1] Bradley Birkelo[2] and Erik H. Saenger[1]

[1]*Earth Science Department, ETH Zurich, Switzerland. E-mail: nima.riahi@erdw.ethz.ch*
[2]*Spectraseis, Denver, CO, USA*

SUMMARY

Theoretical work and modelling studies have led to the hypothesis that the ambient seismic wave field on the surface can be affected by hydrocarbon reservoirs (>800 m depth). Several field studies have linked spectral features on the vertical component between 1 and 10 Hz to reservoir locations. However, such evidence has been criticized due to concerns that surface recordings typically contain a large amount of surface wave noise and correlations to hydrocarbon targets could be caused by non-hydrocarbon variables such as topography or weathering layer thickness. In this paper, we suggest a two-step analysis strategy to address such issues. First, spectral power is only averaged over time periods and frequencies where the distribution of polarization attributes show no obvious dominance of a few surface wave sources. An interferometric test reveals differences in the wave field composition between the filtered and unfiltered data. Second, the residual seismic power is correlated to hydrocarbon as well as non-hydrocarbon targets. The correlations are quantitatively compared using rank correlation and bootstrap confidence intervals. The method is illustrated on a passive seismic data set acquired with three-component, broad-band seismometers at the tight-gas Jonah field in Wyoming, USA. We find evidence that the wave field was dominated by a small number of surface sources in all of the data except for the quietest time periods in the low-frequency range 1.5–3.0 Hz. Seismic power within this subset significantly correlates to a published reservoir map but not with a digital elevation model and less so with an infrastructure density map. The investigated hypothesis can thus not be rejected with this data.

Key words: Fourier analysis; Spatial analysis; Interferometry; Probability distributions; Body waves; Surface waves and free oscillations.

1 INTRODUCTION

The continuous ambient seismic wave field is a function of its distributed, uncontrolled sources as well as the earth medium through which their vibrations travel. The source component can in theory be separated from the medium information if the source distribution and source types have certain statistical properties. For uniform source distributions ensemble averages of noise cross-correlations between two signals can be interpreted as the Green's function between those receivers (Wapenaar 2004; Draganov *et al.* 2006). This is used in applications such as crustal tomography (Shapiro *et al.* 2005) or reflector mapping (Draganov *et al.* 2007; Ruigrok *et al.* 2011). Another approach to approximately separate medium effects is the division of spectra from different components. The horizontal-to-vertical spectral ratio (HVSR) technique is a single-station method and therefore not constrained by receiver geometry. It is routinely used in earthquake engineering to characterize the near surface weathering layer (Bard 1999; D'Amico *et al.* 2008; Fah *et al.* 2003; Bard 2010).

Based on previous empirical observations and theoretical studies by different investigators, Lambert *et al.* (2011) recently formulated an explicit hypothesis that the ambient seismic wavefield can be modified by hydrocarbon reservoirs at depth and that these modifications can be detected at the surface. Plausibility for this hypothesis is provided by two observations. First, there is ample evidence for continuous body waves reaching the surface (Roux *et al.* 2005; Gerstoft *et al.* 2008; Koper & de Foy 2008; Koper *et al.* 2009, 2010; Zhang *et al.* 2009; Landes *et al.* 2010; Poli *et al.* 2012) which would have passed the reservoir. Second, hydrocarbon reservoirs are particular inhomogeneities at low-frequencies: active seismic experiments show evidence of increased attenuation (Chapman *et al.* 2006) as well as increased reflectivity (Goloshubin *et al.* 2006) and these phenomena might in fact be linked (Korneev *et al.* 2004; Quintal *et al.* 2011). In a modelling study that combined small-scale poroelastic theory with large-scale viscoelastic simulation, Lambert *et al.* (2012) propagate upward travelling incoherent seismic energy through a hydrocarbon-saturated inclusion and observe that it correlates with spectral attributes on the surface.

Saenger *et al.* (2009) suggest an alternative explanation where non-linear pore effects produce a secondary wavefield of *p* waves. Both explanations predict a change in body wave energy at the surface in an a priori unknown frequency band. Whether these mechanisms would lead to an increase or decrease in ambient seismic amplitudes in the vicinity of a hydrocarbon reservoir is not obvious *a priori*.

A body of empirical evidence collected over the last decade seems to support the hypothesis. Some case studies describe observations of foci at depth obtained by applying the time-reversal principle to array observations of seismic noise (Steiner *et al.* 2008; Witten & Artman 2011; Goertz *et al.* 2012). Most other observations focus on simpler single-station analyses that correlate lateral spectroscopic features with reservoir locations (Dangel *et al.* 2003; van Mastrigt & Al-Dulaijan 2008; Saenger *et al.* 2009; Birkelo *et al.* 2010; Goertz *et al.* 2012). However, such empirical studies have been subject to considerable controversy (Lambert *et al.* 2009a,b; Green & Greenhalgh 2009a,b). Two concerns are commonly brought forth: first, surface waves often dominate the wavefield and it has been suggested that they might completely mask potential body waves (Ali *et al.* 2010). Second, correlations to a reservoir do not confirm the hypothesis if they are in fact caused by non-hydrocarbon variables that are collocated with the reservoir. For instance, in a modelling study Hestholm *et al.* (2006) found that seismic energy can get trapped in topographic ridges and Hanssen & Bussat (2008) observed a correlation between vertical seismic amplitudes and dune height in a passive seismic data set from the Libyan Desert. Shallow geology also affects seismic surface recordings, a phenomenon exploited by the HVSR technique (Fah *et al.* 2003; Bonnefoy-Claudet *et al.* 2006). Yet another factor is the potential effect that the data acquisition schedule can have: certain areas might have been measured during a period where natural or manmade sources were more energetic, leading to an imprint of the acquisition pattern on the seismic attribute map. Weather conditions, in particular wind speed, are also relevant variables to consider in the 1–10 Hz frequency range (Withers *et al.* 1996).

The principal contribution of this paper is to suggest a spectroscopic analysis strategy for passive seismic data sets that objectively addresses the surface wave problem and the risk of correlations to non-hydrocarbon variables. In the first part we reject time periods and frequencies that exhibit relatively high seismic power and laterally anisotropic polarization since these are considered strong indicators for a few surface sources dominating the signal. The impact of surface waves on the analysis is thus reduced. This single receiver analysis does not aim to identify all surface waves but it is easily implementable and poses few processing related constraints on the survey design. An interferometric test confirms that surface waves from a dominating source were removed this way. In the second part the residual seismic power is spatially correlated to a hydrocarbon as well as to several non-hydrocarbon targets. We will test if the correlation to the hydrocarbon target is significant and stronger than to the non-hydrocarbon targets. Since a linear relation cannot be assumed, and to avoid strong sensitivity to outliers, we use the non-parametric rank correlation in combination with bootstrap confidence intervals.

A first data example is given for a passive seismic data set acquired with three-component broad-band seismometers at the tight-gas Jonah field in Wyoming, USA. Seismic power from appropriate sections of the ambient wavefield recordings is first qualitatively compared to the acquisition pattern and then quantitatively correlated to a reservoir parameter map published by DuBois *et al.* (2004), elevation from the National Elevation Data set (Gesch 2007), and an estimated infrastructure-density map. We find that the hypothesis as

formulated by Lambert *et al.* (2011) cannot be empirically rejected with the available data.

2 DATA EXAMPLE

The tight-gas Jonah field in Wyoming, USA, was discovered in 1977 and has since been well studied, with a large body of knowledge available in Robinson & Shanley (2004). The principal hydrocarbon reservoir is the Lance formation, which is comprised of meandering fluvial sandstones intercalated with overbank siltstones and mudstones. The field is bounded by shear faults on the West and South sides and these faults form the updip and lateral trap for the field. The top of the formation lies at 2.4 km depth and dips down towards the Northeast to 2.8 km. The gross thickness increases downdip from 610 to 915 m (DuBois *et al.* 2004). Faults inside the field compartmentalize the reservoir, leading to an overall heterogeneous distribution of hydrocarbons and pressures. Porosity ranges from 8 to 12 per cent and permeability from 0.01 to 0.9 mD. The Jonah field is being actively developed and produced. Operation and production noise in the area include truck traffic, drilling, well-fracture stimulations and compressors. The treeless area has a relatively flat topography and is partly covered with low-growing sagebrush. The surface geology in the survey area is uniform with shales and marlstones of Eocene age (Love & Christiansen 1985). Statics from active seismic surveys in the area typically show small lateral variation, which are often correlated to elevation.

In a passive seismic survey in 2009 December, three-component, broad-band particle velocity seismometers (Nanometrics Trillium T40) were deployed at 235 sites over the Jonah and the neighbouring Pinedale gas fields. The instruments were chosen because they are able to resolve ground velocity below the low-noise model of Peterson (1993) in the frequency range between ocean microseisms and anthropogenic noise. Since the ocean microseism amplitudes vary smoothly within the survey area they can be used to detect sensors, which deviate significantly from their neighbours, either due to coupling issues or bad instrument settings. Three-component geophones could be used as well, provided that their noise floor is sufficiently low after instrument correction.

The survey was acquired in a roll-along fashion with about 60 seismometers operating synchronously for about 2 d per location, set at a sampling rate of 100 Hz. A total of 88 measurement locations were collocated with data points from reservoir parameter maps published by DuBois *et al.* (2004). Fig. 1 shows an aerial map of the survey area with the measurement locations. Temperatures during the survey were below freezing point and did not allow for a thawing of the top soil. There was no notable precipitation and wind speeds remained below 3 m s^{-1} during more than 95 per cent of the acquisition period. The same data set has previously been investigated by Birkelo *et al.* (2011).

3 ANALYSIS STRATEGY

For the purpose of this paper we formulate the hypothesis to be tested as follows: 'the ambient seismic wavefield at the Jonah field surface exhibits variations in body wave power that are due to the subsurface hydrocarbon reservoir'. The objective of this paper is to present a statistical approach with which this hypothesis can be tested.

The hypothesis explicitly considers body waves because only they have the potential to carry information on the deeper subsurface (>800 m) above 1 Hz. The analysis of such potential body
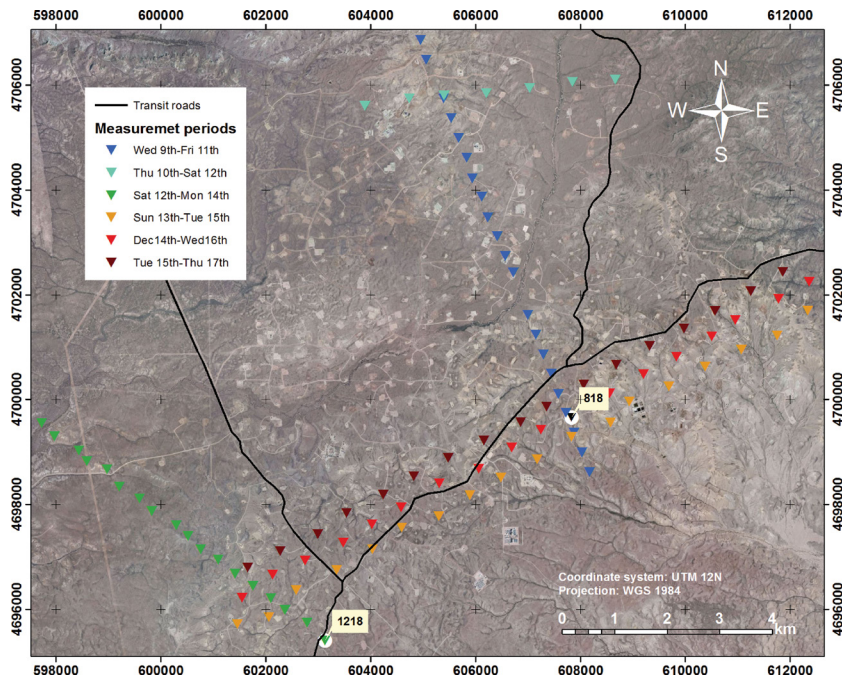
Figure 1. Aerial map of the survey area above the Jonah reservoir. The triangles show the sites where the broad-band seismometers were deployed. The acquisition period is indicated by the colour of the symbols. Recordings from the highlighted locations (1218,818) will be referred to later. The black lines show the transit roads in the survey area.

wave power can be strongly biased by surface wave energy which often dominates the wavefield during a significant fraction or perhaps even all of the recording period. In general, the explicit and unambiguous removal of such surface wave energy requires a full description of the wavefield which in turn necessitates synchronous and non-aliased spatial sampling. Such acquisition designs are hard to implement in a broad-band passive survey for practical reasons. Requirements on spatial sampling can be somewhat relaxed when analysing moveout in cross-correlated receiver gathers. However, this happens at the cost of assuming an isotropic and/or stationary wavefield, which cannot always be guaranteed.

A less ambitious, but more readily implementable solution is to analyse single station polarization statistics to detect and reject time periods and frequencies where one or only a few surface sources dominate the signal. Under reasonable scattering conditions, the vibrations from a surface source seen by a surface receiver at a distance are bound to exhibit a degree of azimuthal directionality, independent of the mixture of wave types and modes involved. Even in the presence of a little more than one dominating source the distribution of polarization produced is likely to remain anisotropic. Because we deployed seismometers in a producing and developing gas field, it can be expected that there are time periods at each recording site where such a small number of surface sources will dominate, either by well pad activity or occasionally passing trucks. Clearly identifiable modes of the distribution of polarization angles over time are therefore a signature of time periods affected by one or a few dominant surface sources and should be rejected.

In the first step of the strategy, we thus identify and select time periods and frequencies where the dominant polarization exhibits lateral isotropy, which is found to be the case for the quietest time periods of the recordings and at low frequencies. This data selection strategy does not strictly achieve a complete removal of surface waves. However, by rejecting time periods and frequencies of high power and obvious azimuthal directivity, we preferentially reject surface waves from nearby surface noise sources and consequently

increase the relative likelihood for the detection of body waves from other distant sources in the remaining data. Also, selecting the lowest power time periods of the wavefield preferentially rejects transients (e.g. truck traffic) resulting in less time variability of the residual wavefield. The seismic power density on the vertical component is then averaged over those time periods and frequencies only. Repeating the process for every measured location gives a map of seismic power density during the quiet time periods with no clearly distinguishable polarization. The concept of focusing on the quietest time periods was also applied by Hanssen & Bussat (2008) and has here been extended to additionally include the requirement for isotropic polarization.

In a second step, this seismic power density is now correlated to a hydrocarbon and as many non-hydrocarbon targets as are available for the measured locations. Correlations are quantified using a rank correlation that only measures monotonic trends without particular assumptions about the type of the relationship (linear or otherwise) and is also more robust against outliers compared to the linear correlation coefficient. Those correlations and their estimated uncertainties are then compared. The non-hydrocarbon variables considered are elevation, well density, and the acquisition pattern.

We test if the correlation to the hydrocarbon target is significant and also whether it is significantly stronger compared to correlations to non-hydrocarbon targets. If this is not the case, the hypothesis as stated above is rejected. Otherwise, the confidence in the hypothesis is increased. Note that empirical studies on observational data alone, which the ambient wavefield inevitably is, cannot be used to verify the causality as stated in the hypothesis.

3.1 Rejection of dominant surface waves

The entire three-component recording is split into non-overlapping small time segments of fixed length, as is usual for the Short-Time Fourier Transform (STFT Gabor 1946). We found a segment length

of $T = 20.48$ s to be short enough to ensure that the stationarity assumption is met within most of those segments, yet long enough to provide reasonable estimates for frequencies down to 0.1 Hz. A 42.5 hr recording thus results in about 7500 time segments. Each of the three components of a segment starting at time t is made to have zero mean, has any linear trend removed (detrending), is tapered with a hanning taper of the same length as the segment, and finally transformed into the complex Fourier domain with the fast Fourier transform (Press 2007)

$$\mathbf{U}(f, t) = [U_E(f, t), U_N(f, t), U_V(f, t)]^T \,, \tag{1}$$

where $U_{E, N, V}(f)$ is the Fourier amplitude as a function of frequency, f, for the east, north and vertical seismometer component, respectively. The segment size of 20.48 s affords a frequency resolution of $1/T = 0.049$ Hz from 0 to 50 Hz. From the Fourier vector $\mathbf{U}(f, t)$ we now estimate the cross-spectral density (CSD) matrix,

$$\hat{\mathbf{S}}(f, t) = k \cdot \mathbf{U}(f, t) \cdot \mathbf{U}^\dagger(f, t) \tag{2}$$

$$k = \frac{2}{f_s \cdot \sum_{\tau=0}^{n-1} |w(\tau)|^2} \,, \tag{3}$$

where $f_s = 100$ Hz is the sampling rate and $w(\tau)$ is the hanning taper applied before the Fourier transform. In this normalization the diagonal elements of $\hat{\mathbf{S}}$ are estimated power spectral densities (PSD) of the three components and the off-diagonal elements are their cross spectral densities. To reduce the statistical noise inherited from the

Fourier amplitudes we compute a weighted time average of eleven adjacent spectral density matrices, with maximum weight for the centre segment, t, and gradually decreasing weights to the flanks. This approach is similar to the commonly used block-averaging technique (Press 2007).

The dominant particle motion at a given frequency and time segment is extracted by the eigenvector of $\hat{\mathbf{S}}(f, t)$ with the largest eigenvalue (Samson 1983; Park *et al.* 1987)

$$\hat{\mathbf{S}}(f, t) \cdot \mathbf{z}_{max}(f, t) = \lambda_{max}(f, t) \cdot \mathbf{z}_{max}(f, t) \,. \tag{4}$$

For a normalized eigenvector the eigenvalue λ_{max} is an estimate of the seismic power density of the dominant polarization. Fig. 2(a) shows λ_{max} as a function of frequency, f, and time, t, for site 1218 (location highlighted in Fig. 1). From acquisition reports as well as from a more detailed analysis of the data (not shown) we know that the recording contains truck traffic, an $M4.1$ earthquake in the Gulf of California, and stationary and non-stationary noise from well operations at less than 120 m distance (hydraulic fracturing, perhaps also well drilling, fluid production or injection). Fig. 2(b) gives the time-series of λ_{max} at $f = 2.15$ Hz for this site. The visible power density variations arise because the above-mentioned sources may contribute different amounts of energy at different times into the 2.15 Hz bin. Fig. 2(c) compares the power spectral density during hand-picked periods where different noise sources were active in the 1218 recording. The large dynamics (power variations up to 50 dB) and frequency dependence of the ambient wavefield are
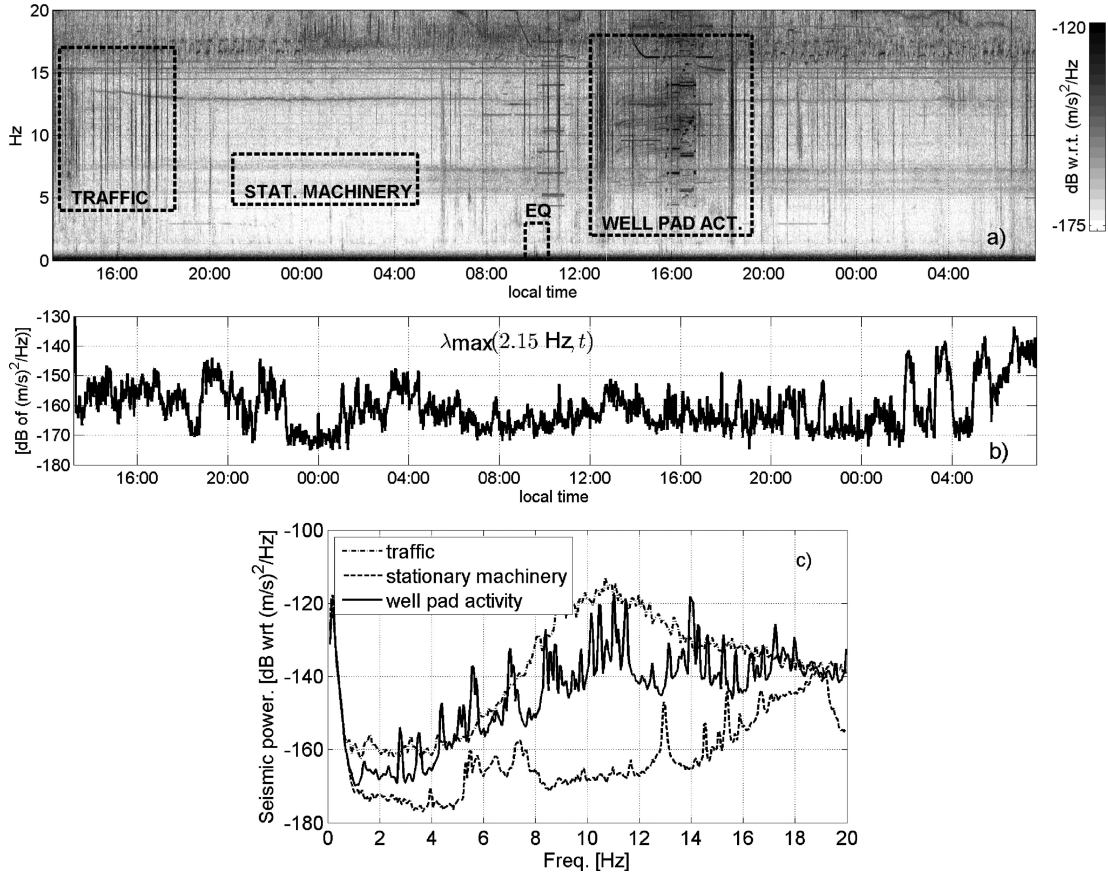

Figure 2. (a) Seismic power density of the dominant polarization, λ_{max}, as a function of frequency and time for the entire recording at site 1218, which was highlighted in Fig. 1 (dark shades indicate higher power). Dashed boxes from left to right identify truck traffic, stationary industrial noise, a $M4.1$ earthquake from the Gulf of California, and industrial well pad activity. (b) Time-series of λ_{max} at the single frequency bin 2.15 Hz. (c) Comparison of power spectral density during hand-picked time periods where different sources dominated.
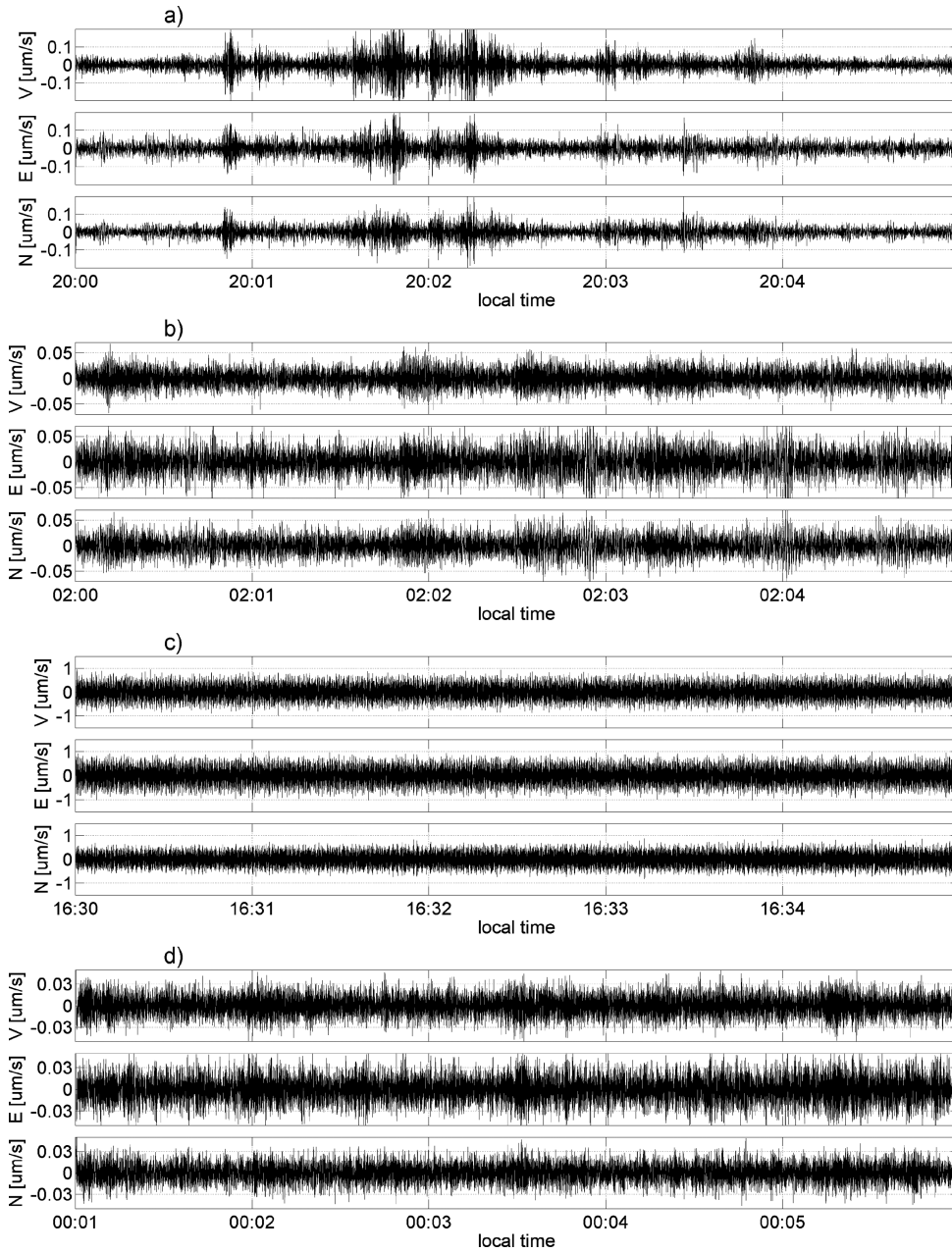
Figure 3. Five minute seismograms of the processes highlighted in Fig. 2(a). V, E and N refer to the vertical, east and north components, respectively. A bandpass filter from 1 to 10 Hz was applied to all signals. (a) Wave train generated by a truck passing outside the local surroundings. (b) Stationary background noise generated by machinery. (c) Stationary background noise generated by well pad activities probably within a 300 m perimeter. (d) Unidentified stationary background noise. Note the different scales of the vertical axes.

illustrated. Nearby road traffic clearly dominates other noise sources. Fig. 3 gives 5 min examples of the three-component seismograms for some of the features highlighted in Fig. 2(a). The shown seismograms are typical for the measurements on the Jonah field. Visual inspection of the seismograms in Figs 3(b)–(d) confirms the stationarity assumption to the first order. The truck traffic shown in Fig. 3(a) is clearly non-stationary on a minute-scale, but the transient nature of such sources makes them relatively easy to identify.

The three complex elements of $\mathbf{z}_{\max}(f, t)$ give the amplitudes and phases of three sinusoidal oscillations in the E, N and V directions with the same frequency. A sketch of the resulting elliptical motion is shown in Fig. 4. The semi-major axis, **a**, and the semi-minor axis,

b, are found by maximizing the length of $\mathrm{Re}[\mathbf{z} \cdot e^{i\xi}]$ using a grid search over $\xi \in [0, \pi)$

$$\xi_0 = \max_{\xi \in [0\,\pi)} \mathrm{Re}\,[\mathbf{z} \cdot \exp(i\xi)] \tag{5}$$

and then setting (Vidale 1986)

$$\mathbf{a} = \mathrm{Re}[\mathbf{z} \cdot e^{i\xi_0}]\,, \tag{6}$$

$$\mathbf{b} = \mathrm{Re}[\mathbf{z} \cdot e^{i(\xi_0 + \pi/2)}]\,. \tag{7}$$

We now define three features of the polarization. The azimuth, $\phi \in [-180°, 180°]$, as the angle between north and the projection of the upward pointing semi-major axis, **a**, to the horizontal plane,
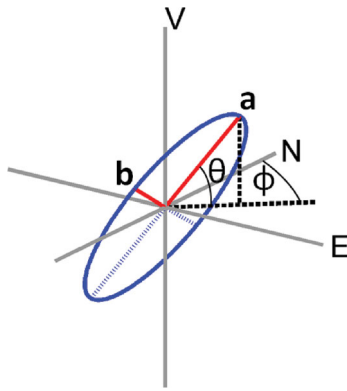
Figure 4. The dominant particle motion is estimated at each frequency by a polarization ellipse. This plot shows the semi-major axis, **a**, the semi-minor axis, **b**, the azimuth angle, ϕ, and the dip angle, θ.

measured clockwise. The dip, $\theta \in [0°, 90°]$, is defined as the angle that the upward pointing semi-major axis spans with the horizontal plane (see Fig. 4). Finally, the reciprocal ellipticity $\rho \in [0, 1]$ is defined as $|\mathbf{b}|/|\mathbf{a}|$. Linear and circular polarization are represented by $\rho = 0$ and $\rho = 1$, respectively, while values in between imply elliptic motion. These three features are computed for all frequencies and all time segments.

For each frequency bin, f_0, we now take the 10 per cent of time segments with the weakest seismic power density. This means that from the power density estimates at f_0 of the full recording we only consider those below the 10th percentile, which for the Jonah recordings corresponds to an effective duration of 4.2–4.8 hr. Based on these segments we compute a histogram of the azimuth with equal-sized bins from $-180°$ to $180°$. The histogram values are normalized such that they integrate to one, whereby we get the empirical probability density function (PDF) of ϕ at frequency f_0 for the quietest time periods. Repeating this process for all frequencies gives a spectrum of such PDFs. Fig. 5(a) shows the result for the frequency range 0–20 Hz. For frequencies above 3 Hz the plot reveals a mostly bimodal distribution of azimuth which changes slowly with frequency (note that the PDFs are periodic in azimuth). The modes are separated by about 180°, as would be expected for surface waves from a distinct direction. This laterally anisotropic polarization property strongly suggests that most of the frequency band above 3 Hz is dominated by surface waves from one or only a few sources. Below 3 Hz these modes disappear and give way to a flat distribution, making this band very unlikely to be dominated by a few sources. Fig. 5(b) gives the same visualization for polarization dip. Dark shades at low angles indicate dominant horizontal particle motion. Frequencies below 0.8 Hz show such dominant horizontal motion, probably due to oceanic microseisms. A concentration of low dips is also visible over most of the frequency band from 4 to 16 Hz, but less so for the frequency range 1–3 Hz. Fig. 5(c) gives the same visualization for reciprocal ellipticity. Except for some narrow-bands, the frequency range from 4 to 14 Hz exhibits polarizations far from linear. Between about 1 and 3 Hz, however, the ellipticites indicate a more isotropic particle motion. Finally, Fig. 5(d) shows the visualization for power density. There is a low-power regime in the frequency range bounded by the oceanic microseisms around 1 Hz and noise processes above 5 Hz.

The above features are specific to the low-power time segments. Fig. 6 gives PDF spectra of polarization parameters and seismic power density when considering time periods with λ_{max} values below the 50th percentile level. Note how the azimuth PDFs for this segment group have stronger modes which now extend down to 0.5 Hz, indicating that also the low frequencies are now dominated by a small number of surface sources even though we still reject 50 per cent of the data. Dominant horizontal motion is observed up to 15 Hz, including the frequency band 0.8–4 Hz, which showed considerably lower probability density values during the quietest 10 per cent of the data, indicating that the signal now contains more horizontally polarized energy. Also, the reciprocal ellipticity in the band 1–3 Hz is less random than for the quiet subset of the data with a bias towards circular polarization.

Using a random number generator we produced three independent time-series of 48 hr of Gaussian, white noise and used them jointly as an isotropic three-component test signal. Fig. 7 gives the polarization PDFs of this synthetic noise. Comparing this plot with Figs 5(a)–(c) qualitatively confirms that the wavefield is roughly isotropic between 0.5 and 3 Hz, and anisotropic almost everywhere else.

Plots as in Figs 5 and 6 were analysed for all 85 measurement locations with valid three-component data within the survey area. We consistently observe such a pattern in the Jonah field: during the 10 per cent quietest time periods the ambient wavefield polarization below 3 Hz exhibits lateral isotropy. For less quiet time periods this observation did not hold reliably. Note that the value of 10 per cent is data-driven and should be re-evaluated for other data sets. For some receivers, the microseism energy visible at the lower end of the spectrum in Fig. 5(d) occasionally extended up to 1.5 Hz. To avoid such interference we therefore compute the average seismic power density between 1.5 and 3.0 Hz, considering only the 10 per cent quietest time periods at every frequency bin. The resulting power density is denoted by $\bar{P}$ and computed for every location.

The focus on quiet time periods with lateral isotropy is a necessary precaution to avoid obvious surface waves but will not necessarily guarantee an increase of body wave energy relative to surface wave energy. Nevertheless, we tried to qualitatively assess the effect of the procedure on surface wave energy by analysing a line of receivers stretching northwestwards from station 1218 using the noise cross-correlation technique (Wapenaar 2004; Snieder *et al.* 2010). An active well pad is located along that line, close to station 1218. Therefore, the line can be considered to have a source in its stationary zone, ensuring an incident wavefield coverage suitable for interferometry despite the anisotropy in the wavefield.

We compute average cross-correlations of the vertical component of receiver 1218 with itself and all northwestward receivers, up to a distance of 7 km. A two-pole, zero-phase bandpass filter between 1 and 3.5 Hz was applied to the raw data, which was then split into segments of 13 s duration for cross-correlation. Fig. 8(a) shows the averaged trace-normalized cross-correlations during a day time period. A coherent wave train with linear moveout at apparent velocity of 1.0 km s^{-1} is detected. This is consistent with a surface wave that is travelling through station 1218 to all other stations. The fact that this wave train has no correspondence at negative times confirms that the well pad behind station 1218 is the main source of the energy and that there is no energy arriving from the opposite side of the line where also no infrastructure is found. Fig. 8(b) shows an identical analysis on a quiet night time period where the 1–3.5 Hz range showed isotropic polarization. No coherent surface wave train is visible. It is therefore clear that the selection of the quietest 10 per cent of the data can provide a means to reduce surface waves from the data.

The presented cross correlation test merely serves as an independent confirmation of the effectiveness of the data selection strategy
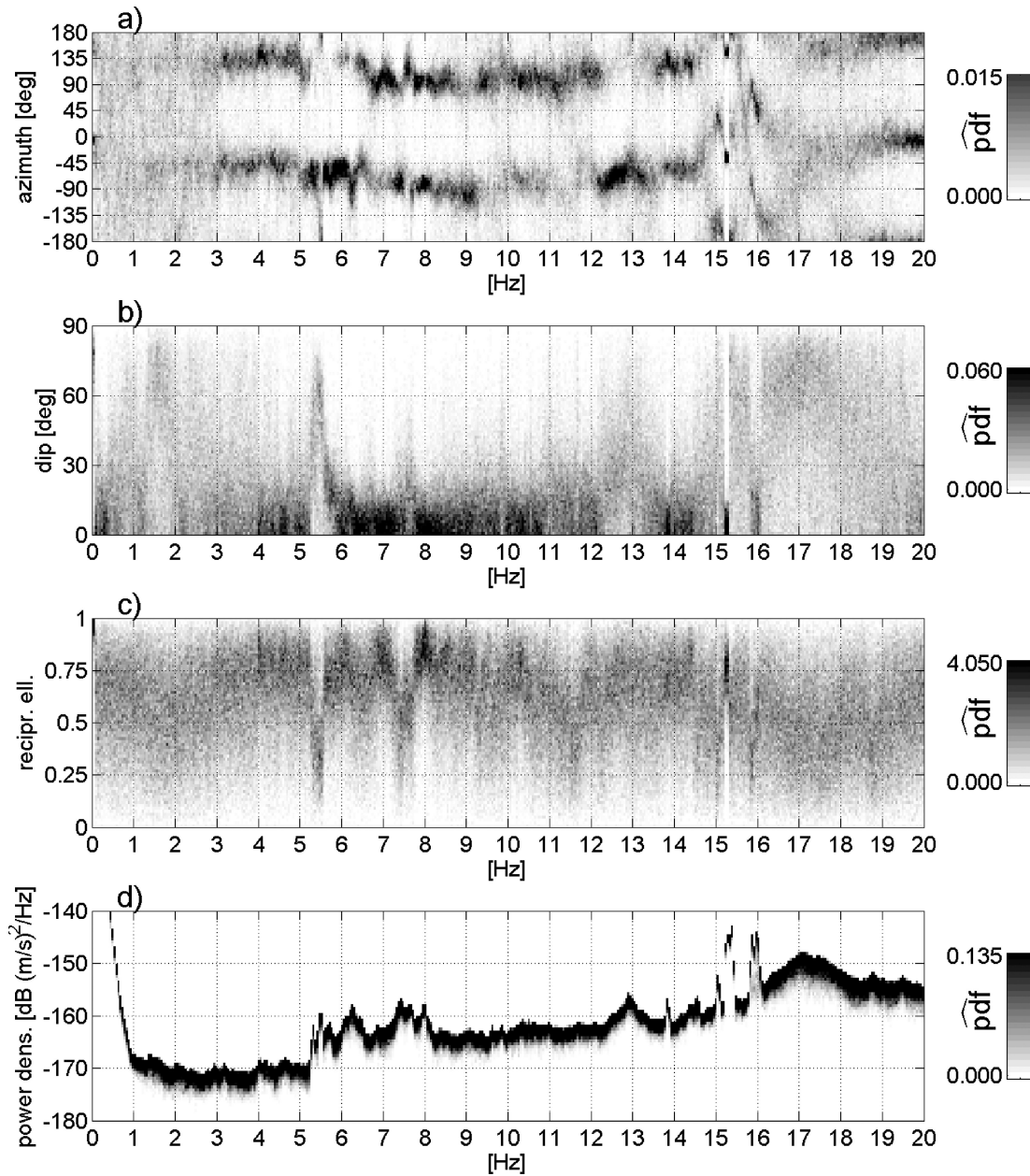
Figure 5. (a) Spectrum of azimuth PDFs from 0 to 20 Hz from site 1218, based on time segments with power density below the 10th percentile of all estimates. Below 3 Hz the PDFs are almost flat. (b) Same visualization for polarization dip. Below 1 Hz there is an increase in horizontal motion (dip < 30°), probably due to oceanic microseisms. (c) Same visualization for reciprocal ellipticity (0: linear polarization, 1: circular polarization). (d) Same visualization for the power density.

with respect to reducing the influence of surface waves on our data. Owing to the observed anisotropy of the incident wavefield over the used time span, it does not provide any additional discriminant between surface and body waves. Indeed, noise cross-correlations in Jonah often did not converge within the available recording period. A coherent event with near zero lag is visible up to about 4.5 km in Fig. 5(a). It might have been generated by broad-side arrivals of surface waves, although a clear polarization from that direction is missing in Fig. 5(a). An alternative explanation would be near-vertically travelling teleseismic body waves, e.g. of oceanic origin (Gerstoft *et al.* 2008; Zhang *et al.* 2009; Landes *et al.* 2010; Poli *et al.* 2012).

Furthermore, the data selection method by means of the power percentile does not ensure synchronous time windows over sev-

eral locations and operates on a per-frequency basis. The cross-correlations of the quiet 4 hr nighttime window shown in Fig. 8(b) are therefore only approximating the actual data that is used to compute $\bar{P}$.

3.2 Quantitative comparison of correlations

Fig. 10 shows the average seismic power density, $\bar{P}$, as computed in the previous section (shaded circles). The measured $\bar{P}$ does not correlate qualitatively to the acquisition schedule indicated in Fig. 1. The sites with high $\bar{P}$ values where the north–south line and the three east–west lines to the South cross were acquired within a time span of 7 d. Sites in the southwest corner of the area where the lowest values of $\bar{P}$ occur were acquired over a time span of 5 d including
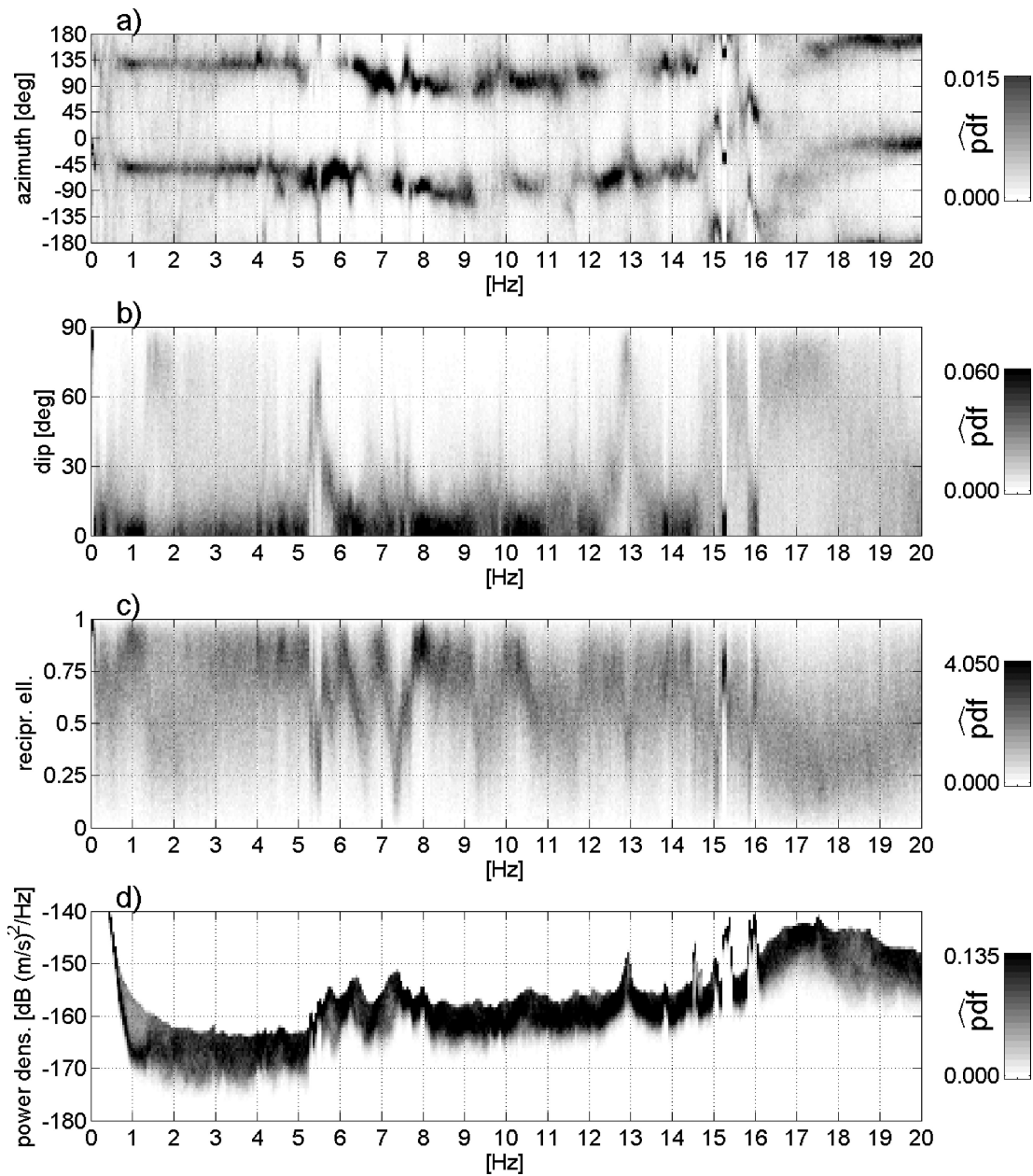
Figure 6. (a) Spectrum of azimuth PDFs from 0 to 20 Hz from site 1218, based on time segments with power density below the 50th percentile of all estimates. The PDFs show distinct modes down to almost 0.5 Hz. (b) Same visualization for polarization dip. Horizontal motion dominates up to about 15 Hz. (c) Same visualization for reciprocal ellipticity (0: linear polarization, 1: circular polarization). The readings vary strongly but there is a trend towards more circular-like polarization. (d) Same visualization for the power density.

both a weekend and the beginning of a workweek. On the north–south line there are two station pairs that are separated by 60 m (northern part) and 85 m (southern part) which show seismic power variations of 2 and 1.7 dB, respectively. Fig. 1 shows the location of reference station 818, which recorded during 9 d. We computed the average seismic power during the 10 per cent quietest periods for each day individually and plot the resulting time-series in Fig. 9. The power variations are contained within a range of about 2 dB, which is of the same order of differences observed at the station pairs near the line crossings. It is unclear to what extent the observed variations between the lines are a short-range phenomenon or a day-to-day effect. However, in relation with the total attribute dynamics of over 10 dB, this variation is modest. The spatial consistency of $\bar{P}$

is another indication that the natural background wavefield during the acquisition period did not change significantly over time.

We now correlate $\bar{P}$ with one hydrocarbon and two non-hydrocarbon targets and compare those correlations. The first target is a reservoir hydrocarbon pore thickness ($S_g\phi H$) map in feet adapted from DuBois *et al.* (2004), also shown in Fig. 10. This variable is a multiplication of estimated porosity, thickness, and hydrocarbon saturation of the reservoir layer and represents a relevant hydrocarbon target. The second target is an elevation map in meters retrieved from the National Elevation Dataset of the U.S. Geological Survey (Gesch 2007), shown in Fig. 11. This map will be used to test for near-surface geology influence. The rationale behind this choice is given in the discussion. Third, a well pad density map
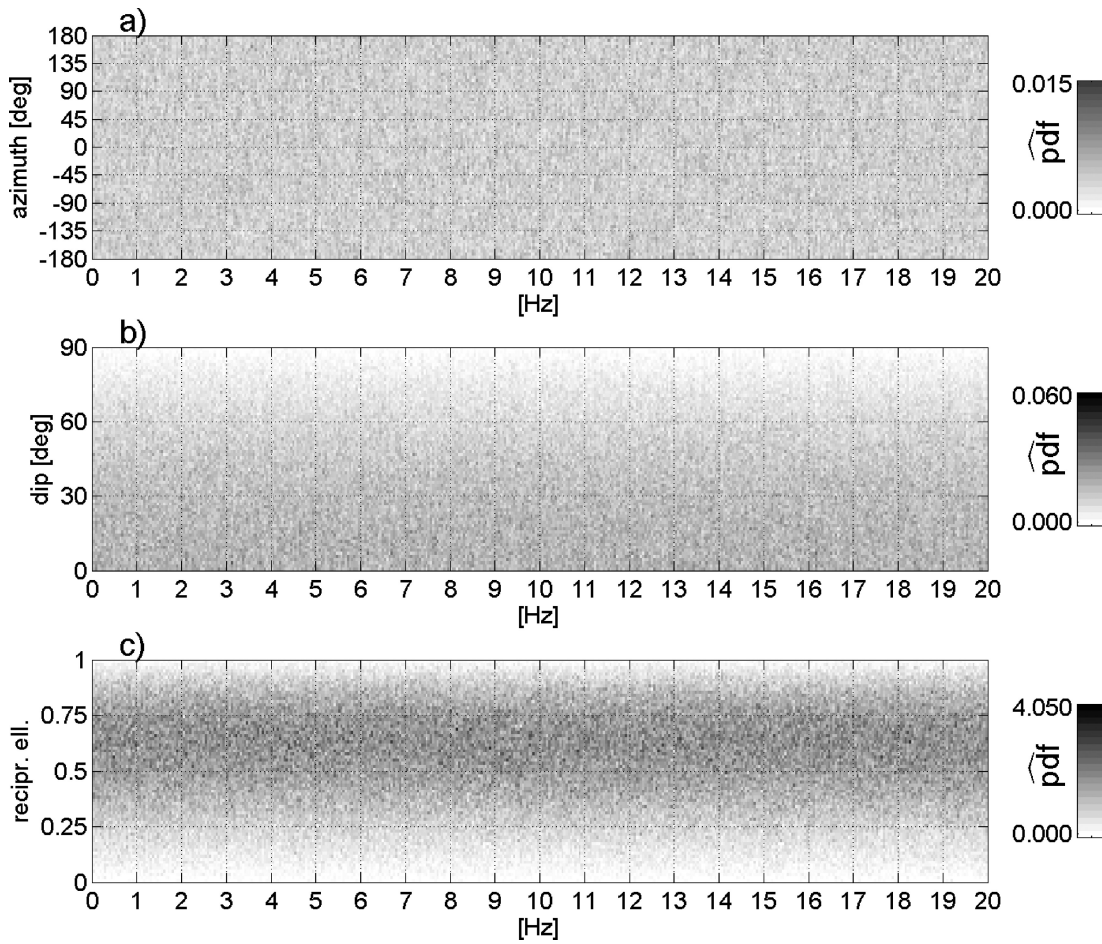
Figure 7. (a) Spectrum of azimuth PDFs from 0 to 20 Hz from Gaussian, white, isotropic noise based on data of equal length as in Fig. 5. (b) Same visualization for polarization dip. Note that the PDF scales as $\cos(\theta)$. (c) Same visualization for reciprocal ellipticity. The isotropic PDF is slightly skewed towards 1, with a mean value of $\rho = 0.57$.

shown in Fig. 12 is used. The latter target is unitless and used as an infrastructure noise proxy where we considered well pads as potential surface wave sources that could radiate seismic energy within a range of about 500 m at about 2 Hz. The radius of 500 m is based on approximate observations of noise decay from machinery noise and the interferometry test. The map was modelled by placing 2-D Gaussian functions with standard deviation 250 m at all well locations and summing them up. Well pad locations as of 2009 were provided by field operators. Strictly speaking, the radius is a function of well pad type, noise environment, and near surface geology, among other factors. The map we use here is therefore primarily interpreted as representing a well density rather than expected seismic noise power due to the wells.

Fig. 13(a) shows $\bar{P}$ plotted against total hydrocarbon pore thickness, $S_g\phi H$. The crossplot exhibits some degree of non-linearity, perhaps two separate trends (dashed lines). Quantifying the relationship with the conventional linear Pearson correlation coefficient might thus give misleading results. Instead, we use the non-parametric Spearman rank correlation coefficient ρ_{rank} (Spearman 1904). This coefficient quantifies to what degree a monotonic relationship exists between two variables, independent of the type of that relationship. It is also more robust with respect to outliers. It ranges from -1 (monotonically decreasing) to $+1$ (monotonically increasing) with values close to zero indicating no monotonic relation between the variables. To compute this measure the values of a variable are re-

placed by their rank relative to the other values in that variable: the lowest value is replaced by 1, the second lowest by 2, and so on. In Fig. 14(a) (left-hand panel) the such transformed versions of $\bar{P}$ and $S_g\phi H$ are plotted against each other. The rank correlation is the conventional correlation coefficient computed on the ranks. The grey line in the panel shows the corresponding trend.

To include the uncertainty in the analysis, we do not estimate a single coefficient, but rather a confidence interval within which ρ_{rank} lies. This is attained by repeatedly estimating ρ_{rank} based on 1000 bootstrap resamples of the scatter points. From this resampling distribution a bias-corrected and accelerated 90 per cent bootstrap confidence interval is computed (Efron & Tibshirani 1993).

Fig. 14(a) (right-hand panel) shows the resulting distribution of ρ_{rank}. There exists a significant positive relation between $S_g\phi H$ and $\bar{P}$, as testified by the 90 per cent confidence interval $\rho_{rank} \in [0.43, 0.67]$. Fig. 14(b) gives the same plots for $\bar{P}$ and elevation, with $\rho_{rank} \in [-0.16, 0.24]$. Note that the confidence interval contains zero and therefore no significant monotonic relation can be claimed at the 90 per cent level. Fig. 14(c) shows the plots for $\bar{P}$ and well density, with $\rho_{rank} \in [0.06, 0.38]$. There is a weak relationship, but one that is significantly weaker than the one to the hydrocarbon target.

Since the hydrocarbons in Jonah are mined we expect a certain correlation between the hydrocarbon target and infrastructure. In our data example the 90 per cent confidence interval of the rank
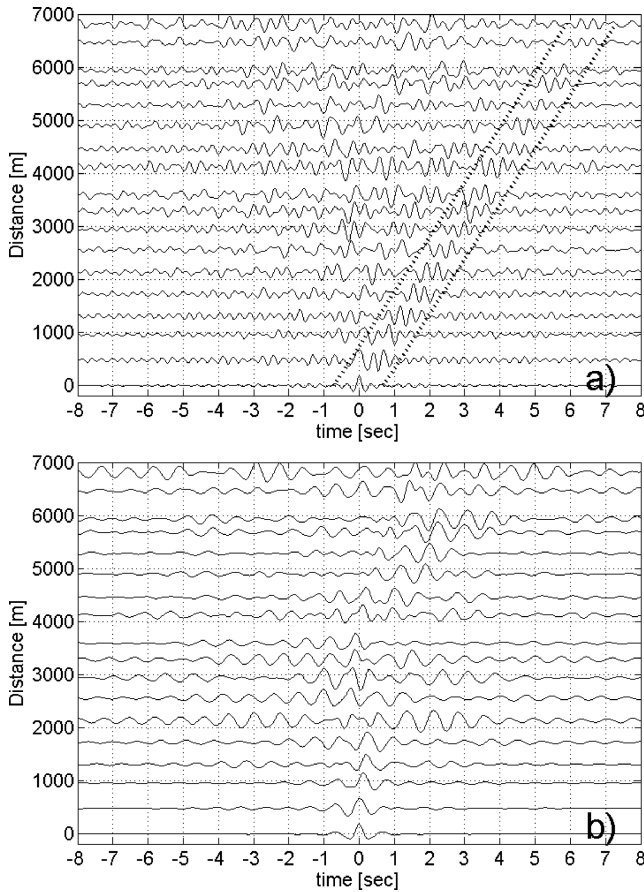
Figure 8. (a) Average noise cross-correlations of the vertical component of receiver 1218 with 18 receivers stretching out 7 km northwestwards from station 1218. All traces were normalized to unity. This panel shows daytime recordings (1500h–1700h local time) which were bandpass filtered between 1 and 3.5 Hz. The traces are normalized and centred at the distance of the receiver to station 1218. The dotted lines highlight a coherent wave train with a linear moveout at apparent velocity 1.0 km s^{-1}, most probably caused by a surface wave. (b) Same as (a) but using night time recordings (0100h–0500h local time) where polarization was laterally isotropic. No coherent moveout can be detected.

correlation between $S_g\phi H$ and well density is $\rho_{\text{rank}} \in [0.31, 0.62]$. The fact that the attribute correlates better to the reservoir than it does to the confounder, while the confounder itself correlates well to the reservoir suggests that there is a different nature between these
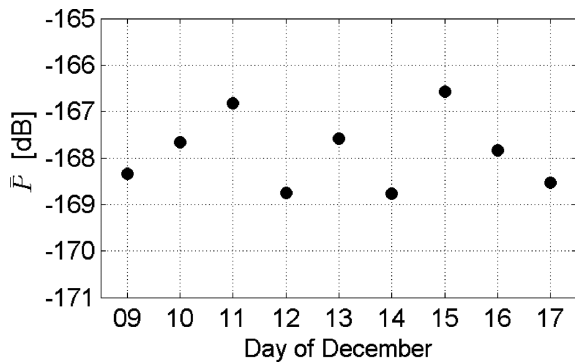

Figure 9. Average seismic power during the quietest 10 per cent of time periods during consecutive 24-hr segments of the recording from reference station 818. The temporal variations are within a range of roughly 2 dB.
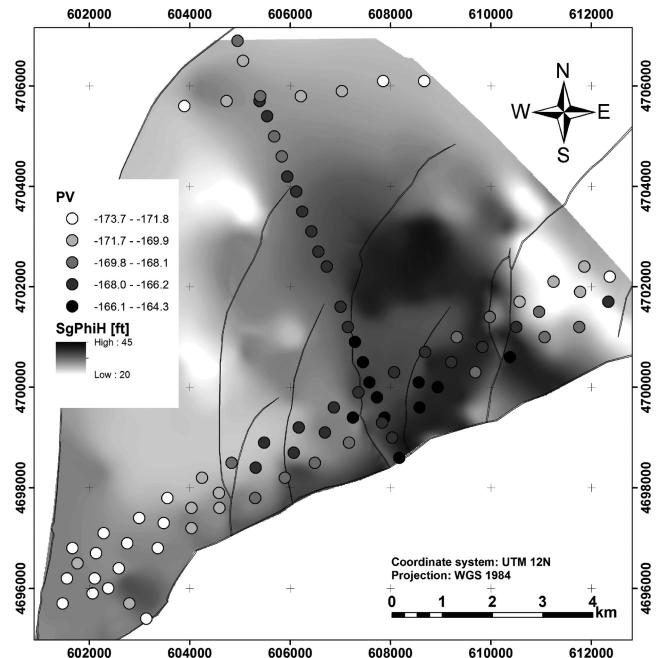

Figure 10. Contoured map of hydrocarbon pore thickness, $S_g\phi H$, of the Jonah reservoir adapted from DuBois *et al.* (2004). The shaded circles show $\bar{P}$, the average seismic power density within 1.5–3.0 Hz during the quietest 10 per cent of the recording [dB w.r.t. (m s^{-1})^2 Hz^{-1}].
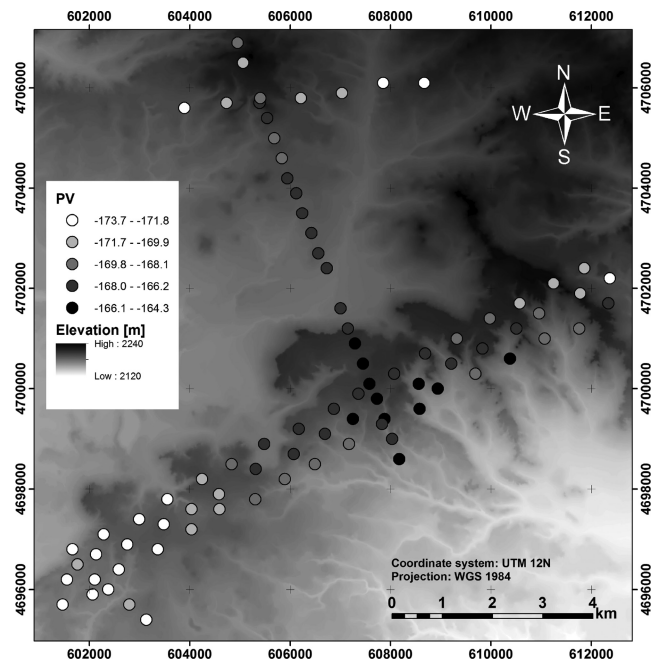

Figure 11. Elevation map at the Jonah field from the National Elevation Dataset (Gesch 2007). The shaded circles show $\bar{P}$, the average seismic power density within 1.5–3.0 Hz during the quietest 10 per cent of the recording [dB w.r.t. (m s^{-1})^2 Hz^{-1}].

correlations. Specifically, the low $S_g\phi H$ values in the Southwest corner are captured better by the attribute, while contrasting with existing well pads there.

The above analysis was restricted to the quietest 10 per cent of the recording durations. We also investigated how the rank correlations change as we used different amounts of data, from 2 per cent to 100 per cent. Fig. 15(a) shows the resulting rank
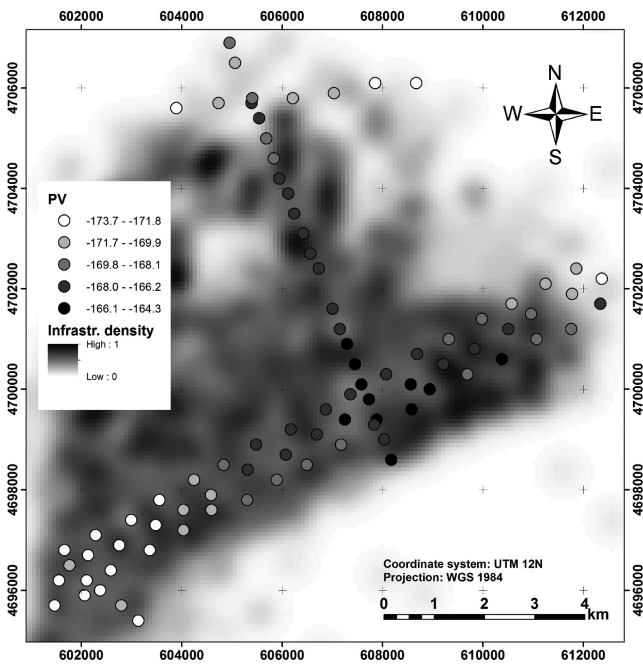
Figure 12. Well pad density map at the Jonah field. This map is used as a proxy for anthropogenic noise. The shaded circles show $\bar{P}$, the average seismic power density within 1.5–3.0 Hz during the quietest 10 per cent of the recording [dB w.r.t. $(\mathrm{m\,s^{-1}})^2\,\mathrm{Hz^{-1}}$].

correlation to the reservoir is observed, there is no correlation to well density. All plots in Fig. 15 use the same colour-scale.

4 DISCUSSION

We have computed the average seismic power density of the ambient wavefield polarization at the Jonah tight-gas field in the frequency range 1.5–3.0 Hz, restricted to the 10 per cent quietest time periods. This subset has low-power, is laterally isotropic and is likely to represent the isotropic, quasi-stationary background wavefield that consists of a mixture of body waves and surface waves originating from an apparently isotropic source distribution. Although the ratio of surface to body waves is unknown, filtering the wavefield in this way increases the chance of uncovering weak components that may carry information about the deeper subsurface. An interferometric test independently confirms that the data selection strategy can indeed lead to a significant attenuation of surface waves from a specific direction.

The seismic power density correlates well with hydrocarbon pore thickness published by DuBois *et al.* (2004). The same seismic attribute does not correlate to an elevation map and only weakly correlates to an estimated well density map. Also, no qualitative relation is visible to the data acquisition pattern that spanned 7 d. This is confirmed by the observation that day-to-day temporal variations of $\bar{P}$ were much smaller than the observed lateral variations (Fig. 9).

The above three variables are thus unlikely to confound the correlation to the reservoir parameter map and we have a situation where the hypothesis cannot be rejected at this stage. However, other non-hydrocarbon variables should still be included. Withers *et al.* (1996) investigated the effect of wind speed on the seismic background noise on a location in New Mexico with similar topography and vegetation. No precipitation occurred during the data acquisition period and wind speeds did not exceed the 3 m s^{-1} threshold above which Withers *et al.* (1996) observed an impact on seismic background noise on the surface for a similar topography. A significant atmospheric impact on the analysis is therefore unlikely.

Weathering layer thickness should still be included because of its well-known influence on particle motion. Information on the near-surface geology in Jonah is very limited. The HVSR technique may still be used to estimate lateral variations of near-surface geology (Goertz *et al.* 2012). However, an analysis of H/V spectra in the
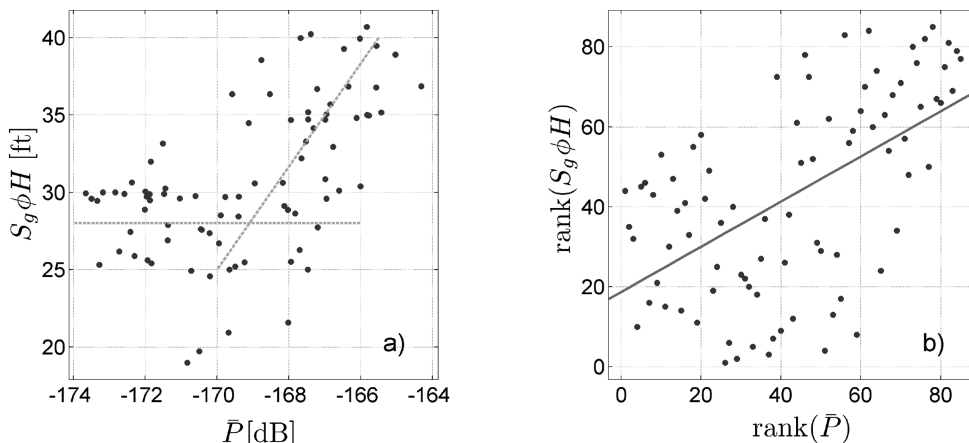
correlations colour-coded as a function of frequency and percent of data used. The colour-scale is white for insignificant correlation at the 90 per cent significance level, which for 85 data points corresponds to $|\rho_{\mathrm{rank}}| < 0.18$, and gradually saturates to blue or red for $\rho_{\mathrm{rank}} \geq 0.55$ and $\rho_{\mathrm{rank}} \leq -0.55$, respectively (strongest observed absolute correlations). Strongest correlations exist in the frequency range 1.5–3.0 Hz for up to about 50 per cent of the data being used. Note that when using more than 10 per cent of the data the necessary isotropy is not present. Weaker correlations also occur between 6 and 15 Hz. Correlations to elevation (Fig. 15b) are mostly insignificant. Significant correlation to well density is observed in the frequency range 6–12 Hz (Fig. 15c) and corresponds to the weaker correlations to $S_g\phi H$ in the same band, confirming a common concern that correlations to reservoirs are confounded by infrastructure noise. However, in the 1–4 Hz range, where best

Figure 13. (a) The hydrocarbon target values $S_g\phi H$ are plotted against $\bar{P}$. The scatter exhibits a slight non-linearity, potentially two separate trends (dashed lines). The relation should not be described with the linear correlation coefficient. (b) The ranks of $S_g\phi H$ are plotted against the ranks of $\bar{P}$. The rank correlation in this case is the linear correlation in the ranks and quantifies the degree of monotonic relation between the two variables (grey line is best linear fit).
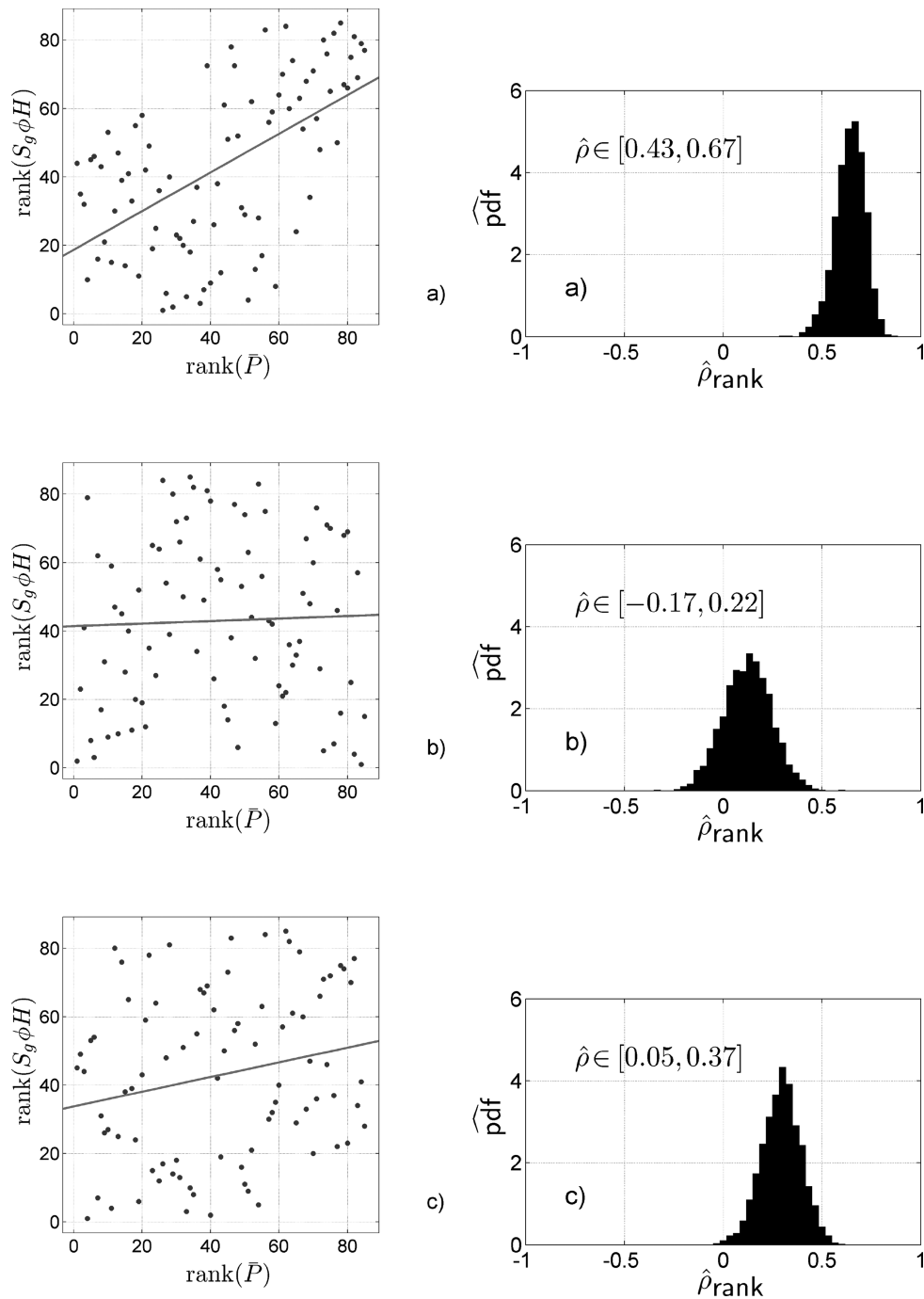
Figure 14. (a) Ranks of $S_g\phi H$ plotted against ranks of $\bar{P}$ (left-hand panel) and bootstrap distribution of the estimated rank correlation coefficient ρ_{rank} (right-hand panel). The 90 per cent confidence interval for the rank correlation is given in the right-hand panel. (b) Same plots for elevation against $\bar{P}$. (c) Same plots for well density against $\bar{P}$.

measured locations showed that they were largely controlled by source characteristics, rendering them unusable for site characterization. No statics from active seismic surveys were available to us, but based on experience from the wider area, they often correlate with elevation. In this context, we used the elevation map as the closest available proxy for near-surface geology.

The well pad density map as a proxy for anthropogenic seismic noise should be considered with caution since it is based on the assumptions that each well isotropically radiates the same amount of surface wave energy during the analysis period and that the noise decay with distance does not depend on location. We use it in this

work mainly to illustrate how infrastructure noise could be included in a comparative correlational analysis. Alternative proxies based on field logs of surface activity and dedicated seismic characterization of noise sources around the field would be preferable. Energy from near-by road traffic is unlikely to affect the quietest time periods, since this would require such transient events to occur during more than 90 per cent of the recording period. The selected attribute also shows no visual relation to the transit roads in Fig. 10.

The bootstrap method is likely to generate somewhat optimistic confidence intervals because the considered variables have a certain degree of spatial smoothness. A more appropriate method to use in
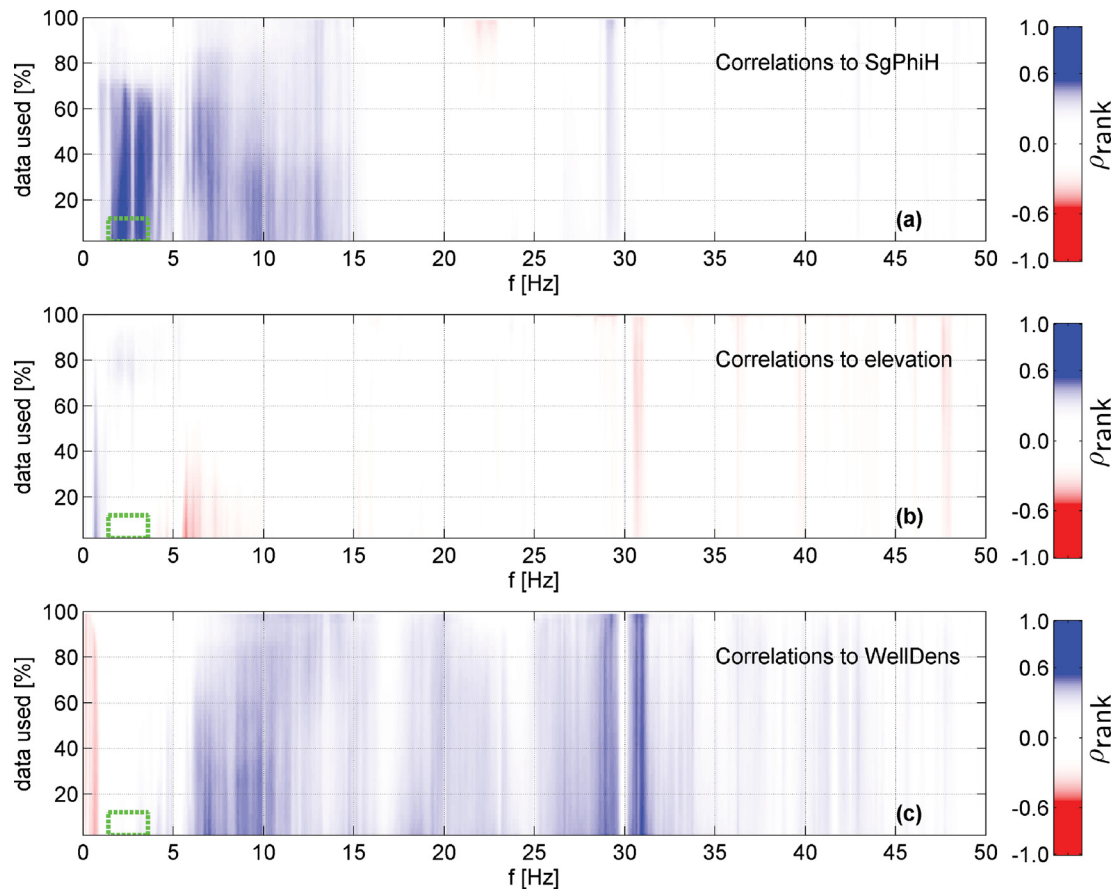
Figure 15. (a) The seismic power density at different frequencies is averaged over progressively larger percentages of the recording (from quietest time periods to the entire recording) and then correlated to $S_g\phi H$. The graph shows the rank correlation coefficient colour-coded as a function of frequency and percentage of data used. The colourmap is white where the correlation is insignificant. The dashed green box highlights the data that was used in Figs 13 and 14. (b) Same visualization showing rank correlations to elevation. (c) Same visualization showing rank correlations to estimated well density.

such a situation is described by Buhlmann (2002). However, the simple technique used here is sufficient since the relatively high correlation to the subsurface reservoir is likely to hold even with larger confidence intervals and the statement of insignificant or weak correlation to non-hydrocarbon variables is even more supported by larger confidence intervals.

We note again that the lateral isotropy is a necessary but not sufficient requirement to identify subvertically travelling body waves. Noise cross-correlations are an interesting alternative to detect body waves (Draganov *et al.* 2006), but their applicability can be complicated by unsuited ambient source distributions and/or short recording periods. Another alternative to reduce ambiguities in the wavefield analysis is offered by array analysis (Rost & Thomas 2002). Appropriately designed sensor arrays distributed around the area of interest can provide a means to detect subvertically incident body waves directly (Gerstoft *et al.* 2008; Koper *et al.* 2009; Zhang *et al.* 2009; Birkelo *et al.* 2010).

5 CONCLUSIONS

Providing empirical evidence for the hypothesis that the ambient seismic wavefield above 1 Hz carries information about the deeper subsurface (>800 m) is hampered by (i) uncontrolled surface wave sources and (ii) influences of the near-surface geology. Both effects can confound correlations of observed attributes to deeper targets.

In this work, we suggest a strategy that addresses these issues in two main steps. First, we only average seismic power density over

frequencies and time periods where the dominant polarization has low power and is laterally isotropic. This is considered a minimum criterion to reduce surface wave interferences from a few dominant sources. Second, we test whether the residual seismic power density significantly correlates to a hydrocarbon target and that this correlation is stronger than correlation to non-hydrocarbon targets. We recommend to do this quantitatively using the non-parametric rank correlation and bootstrap confidence intervals.

A first example for the proposed strategy is given for an ambient wavefield data set acquired over a producing tight-gas field. We find that the quietest 10 per cent of time periods in the 1.5–3.0 Hz band meet the minimum requirements against few dominating surface sources. Seismic power density in this subset significantly correlates to a hydrocarbon pore thickness map, while it does not significantly correlate to elevation, only weakly correlates to an estimated well density, and shows no apparent relation to the data acquisition days. We can therefore not falsify the hypothesis that the ambient wavefield contains a measurable amount of body wave energy carrying information about the subsurface hydrocarbon target.

REFERENCES

Ali, M.Y., Berteussen, K.A., Small, J. & Barkat, B., 2010. Low-frequency passive seismic experiments in Abu Dhabi, United Arab Emirates: implications for hydrocarbon detection, *Geophys. Prospect.,* **58**(5), 875–899.

Bard, P.Y., 1999. *Microtremor Measurements: A Tool for Site Effect Estimation?,* pp. 1251–1279, Balkema, Rotterdam.

Bard, P.Y., 2010. *From Non-invasive Site Characterization to Site Amplification: Recent Advances in the Use of Ambient Vibration Measurements,* Chapter 5, pp. 105–123, Geotechnical, Geological, and Earthquake Engineering 17.

Birkelo, B., Duclos, M., Artman, B., Schechinger, B., Witten, B., Goertz, A., Weemstra, K. & Hadidi, M., 2010. A passive low-frequency seismic survey in Abu Dhabi – Shaheen project, *SEG Tech. Prog. Expanded Abstracts,* **29**(1), 2207–2211.

Birkelo, B., Goertz, A., Cieslik, K. & LaBarre, E., 2011. Locating high-productivity areas of tight gas-sand reservoirs using LF seismic surveys, in *Proceedings of the EAGE 77th Annual International Meeting,* Expanded Abstracts, Vienna, pp. C016.

Bonnefoy-Claudet, S., Cotton, F. & Bard, P.-Y., 2006. The nature of noise wavefield and its applications for site effects studies: a literature review, *Earth Sci. Rev.,* **79**, w205–227.

Buhlmann, P., 2002. Bootstraps for time series, *Stat. Sci.,* **17**(1), 52–72.

Chapman, M., Liu, E.R. & Li, X.Y., 2006. The influence of fluid-sensitive dispersion and attenuation on AVO analysis, *Geophys. J. Int.,* **167**(1), 89–105.

D'Amico, V., Picozzi, M., Baliva, F. & Albarello, D., 2008. Ambient noise measurements for preliminary site-effects characterization in the urban area of Florence, Italy, *Bull. Seism. Soc. Am.,* **98**(3), 1373–1388.

Dangel, S., Schaepman, M.E., Stoll, E.P., Carniel, R., Barzandji, O., Rode, E.D. & Singer, J.M., 2003. Phenomenology of tremor-like signals observed over hydrocarbon reservoirs, *J. Volc. Geotherm. Res.,* **128**(1-3), 135–158.

Draganov, D., Wapenaar, K. & Thorbecke, J., 2006. Seismic interferometry: reconstructing the Earth's reflection response, *Geophysics,* **71**(4), Si61–Si70.

Draganov, D., Wapenaar, K., Mulder, W., Singer, J. & Verdel, A., 2007. Retrieval of reflections from seismic background-noise measurements, *Geophys. Res. Lett.,* **34**(L04305), doi:10.1029/2006gl028735.

DuBois, D.P., Wynne, P.J., Smagala, T.M., Johnson, J.L., Engler, K.D. & McBride, B.C., 2004. *Geology of the Jonah Field, Sublette County,* Wyoming, AAPG Studies in Geology.

Efron, B. & Tibshirani, R., 1993. *An Introduction to the Bootstrap,* Monographs on Statistics and Applied Probability, Chapman and Hall, New York.

Fah, D., Kind, F. & Giardini, D., 2003. Inversion of local S-wave velocity structures from average H/V ratios, and their use for the estimation of site-effects, *J. Seismol.,* **7**(4), 449–467.

Gabor, D., 1946. Theory of communication, *J. Inst. Elec. Eng.,* **93**, 429–457.

Gerstoft, P., Shearer, P.M., Harmon, N. & Zhang, J., 2008. Global P, PP, and PKP wave microseisms observed from distant storms, *Geophys. Res. Lett.,* **35**(L23306), doi:10.1029/2008gl036111.

Gesch, D.B., 2007. *The National Elevation Dataset,* Chapter 4, pp. 61–82, Amercian Society for Photogrammetry and Remote Sensing, Bethesda, MD.

Goertz, A., Schechinger, B., Witten, B., Koerbe, M. & Krajewski, P., 2012. Extracting subsurface information from ambient seismic noise: a case study from Germany, *Geophysics,* **77**(4), 1–19.

Goloshubin, G., VanSchuyver, C., Korneev, V., Silin, D. & Vingalov, V., 2006. Reservoir imaging using low frequencies of seismic reflections, *The Leading Edge,* **25**(5), 527–531.

Green, A.G. & Greenhalgh, S., 2009a. Comment on 'Low-frequency microtremor anomalies at an oil and gas field in Voitsdorf, Austria' by Marc-Andre Lambert, Stefan Schmalholz, Erik H. Saenger and Brian Steiner, *Geophys. Prospect.,* **58**, 335–339.

Green, A.G. & Greenhalgh, S., 2009b. Microtremor spectra: a proven means for estimating resonant frequencies and S-wave velocities of shallow soils/sediments, but a questionable tool for locating hydrocarbon reservoirs, *First Break,* **27**(7), doi:10.3997/1365-2397.2009012.

Hanssen, P. & Bussat, S., 2008. Pitfalls in the analysis of low-frequency passive seismic data, *First Break,* **26**, 111–119.

Hestholm, S., Moran, M., Ketcham, S., Anderson, T., Dillen, M. & McMechan, G., 2006. Effects of free-surface topography on moving-seismic-source modeling, *Geophysics,* **71**(6), T159–T166.

Koper, K.D. & de Foy, B., 2008. Seasonal Anisotropy in Short-Period Seismic Noise Recorded in South Asia, *Bull. Seism. Soc. Am.,* **98**(6), 3033–3045.

Koper, K.D., de Foy, B. & Benz, H., 2009. Composition and variation of noise recorded at the Yellowknife Seismic Array, 1991-2007, *J. Geophys. Res.-Solid Earth,* **114**(B10310), doi:10.1029/2009jb006307.

Koper, K.D., Seats, K. & Benz, H., 2010. On the composition of Earth's short-period seismic noise field, *Bull. Seism. Soc. Am.,* **100**(2), 606–617.

Korneev, V.A., Goloshubin, G.M., Daley, T.M. & Silin, D.B., 2004. Seismic low-frequency effects in monitoring fluid-saturated reservoirs, *Geophysics,* **69**(2), 522–532.

Lambert, M., Schmalholz, S.M., Saenger, E.H. & Steiner, B., 2009a. Reply to comment on 'low-frequency microtremor anomalies at an oil and gas field in Voitsdorf, Austria' by Marc-Andre Lambert, Stefan M. Schmalholz, Erik H. Saenger and Brian Steiner, *Geophys. Prospect.,* **58**, 341–346.

Lambert, M.A., Schmalholz, S.M., Saenger, E.H. & Steiner, B., 2009b. Low-frequency microtremor anomalies at an oil and gas field in Voitsdorf, Austria, *Geophys. Prospect.,* **57**(3), 393–411.

Lambert, M.-A., Nguyen, T., Saenger, E.H. & Schmalholz, S.M., 2011. Spectral analysis of ambient ground-motion—noise reduction techniques and a methodology for mapping horizontal inhomogeneity, *J. Appl. Geophys.,* **74**(2-3), 100–113.

Lambert, M.A., Saenger, E.H., Quintal, B. & Schmalholz, S.M., 2013. Numerical simulation of ambient seismic wavefield modification caused by pore-fluid effects in an oil reservoir, *Geophysics,* **78**, doi:10.1190/GEO2011-0513.1.

Landes, M., Hubans, F., Shapiro, N.M., Paul, A. & Campillo, M., 2010. Origin of deep ocean microseisms by using teleseismic body waves, *J. Geophys. Res.-Solid Earth,* **115**(B05302), doi:10.1029/2009jb006918.

Love, J.D. & Christiansen, A.C., 1985. *Geologic map of Wyoming*, U.S. Geological Survey.

Park, J., Vernon, F.L. & Lindberg, C.R., 1987. Frequency-dependent polarization analysis of high-frequency seismograms, *J. Geophys. Res.-Solid Earth Planets,* **92**(B12), 12 664–12 674.

Peterson, J., 1993. Observations and modeling of seismic background noise, US Geological Survey, Albuquerque, New Mexico.

Poli, P., Pedersen, H.A., Campillo, M. & the, P.L.W.G., 2012. Emergence of body waves from cross-correlation of short period seismic noise, *Geophys. J. Int.,* **188**(2), 549–558.

Press, W.H., 2007. *Numerical Recipes: The Art of Scientific Computing, 3rd edn,* Cambridge University Press, Cambridge, UK; New York.

Quintal, B., Schmalholz, S.M. & Podladchikov, Y.Y., 2011. Impact of fluid saturation on the reflection coefficient of a poroelastic layer, *Geophysics,* **76**(2), N1–N12.

Robinson, J.W. & Shanley, K.W., 2004. *Jonah Field : Case Study of a Tight-Gas Fluvial Reservoir,* AAPG studies in geology, American Association of Petroleum Geologists, Tulsa, Oklahoma.

Rost, S. & Thomas, C., 2002. Array seismology: methods and applications, *Rev. Geophys.,* **40**(1008), doi:10.1029/2000rg000100.

Roux, P., Sabra, K.G., Gerstoft, P., Kuperman, W.A. & Fehler, M.C., 2005. P-waves from cross-correlation of seismic noise, *Geophys. Res. Lett.,* **32**(L19303), doi:10.1029/2005gl023803.

Ruigrok, E., Campman, X. & Wapenaar, K., 2011. Extraction of P-wave reflections from microseisms, *Comptes Rendus Geosci.,* **343**(8-9), 512–525.

Saenger, E.H. *et al.*, 2009. A passive seismic survey over a gas field: analysis of low-frequency anomalies, *Geophysics,* **74**(2), O29–O40.

Samson, J.C., 1983. Pure states, polarized waves, and principal components in the spectra of multiple, geophysical time-series, *Geophys. J. R. astr. Soc.,* **72**(3), 647–664.

Shapiro, N.M., Campillo, M., Stehly, L. & Ritzwoller, M.H., 2005. High-resolution surface-wave tomography from ambient seismic noise, *Science,* **307**(5715), 1615–1618.

Snieder, R., Miyazawa, M., Slob, E., Vasconcelos, I. & Wapenaar, K., 2010. *A Comparison of Strategies for Seismic Interferometry,* Arrays and Array Methods in Global Seismology, Springer, New York.

Spearman, C., 1904. The proof and measurement of association between two things, *Am. J. Psychol.,* **15,** 72–101.

Steiner, B., Saenger, E.H. & Schmalholz, S.M., 2008. Time reverse modeling of low-frequency microtremors: application to hydrocarbon reservoir localization, *Geophys. Res. Lett.,* **35**(L03307), doi:10.1029/2007gl032097.

van Mastrigt, P. & Al-Dulaijan, A., 2008. Seismic spectroscopy using ampli-fied 3C geophones, in *Proceedings of the EAGE 70th Annual International Meeting,* Expanded Abstracts, p. B047.

Vidale, J.E., 1986. Complex polarization analysis of particle motion, *Bull. Seism. Soc. Am.,* **76**(5), 1393–1405.

Wapenaar, K., 2004. Retrieving the Elastodynamic Green's function of an arbitrary inhomogeneous medium by cross correlation, *Phys. Rev. Lett.,* **93**(254301), doi:10.1103/PhysRevLett.93.254301.

Withers, M.M., Aster, R.C., Young, C.J. & Chael, E.P., 1996. High-frequency analysis of seismic background noise as a function of wind speed and shallow depth, *Bull. Seism. Soc. Am.,* **86**(5), 1507–1515.

Witten, B. & Artman, B., 2011. Signal-to-noise estimates of time-reverse images, *Geophysics,* **76**(2), MA1–MA10.

Zhang, J., Gerstoft, P. & Shearer, P.M., 2009. High-frequency P-wave seismic noise driven by ocean winds, *Geophys. Res. Lett.,* **36**(L09302), doi:10.1029/2009gl037761.